LARGE AXISYMMETRIC DEFORMATION OF A CYLINDRICAL SHELL CONVEYING A VISCOUS FLOW

M. HEIL AND T. J. PEDLEY

Department of Applied Mathematics, University of Leeds, Leeds LS2 9JT, U.K.

Large axisymmetric deformations of collapsible tubes conveying a viscous flow are examined. Geometrically nonlinear Lagrangian shell theory is used to describe the deformation of the tube. The fluid flow is modelled using lubrication theory. The coupled fluid–solid problem is solved numerically using an FEM technique. In order to explain the mechanisms involved in the tube deformation, the effects of bending stiffness, wall shear stress and axial pre-stretch are examined in detail. The dependence of the tube resistance on the volume flux is investigated for two different experimental set-ups (constant pressure at either upstream or downstream end of the collapsible tube). Finally, the exact nonlinear shell theory used in this paper is compared to Sanders' moderate rotation theory and an improvement to his theory is suggested.

1. INTRODUCTION

THE PROBLEM OF FLOW THROUGH COLLAPSIBLE TUBES has been studied both theoretically and experimentally by many authors [for a recent review see Kamm & Pedley (1989)]. The main motivation for this work comes from the investigation of certain biological flows, such as blood flow in veins and arteries or air flow in the bronchial airways during forced expiration. The tubes collapse when the transmural pressure difference (internal minus external pressure) falls below a critical level. Following the collapse, self-excited oscillations can be observed for a wide range of parameters. So far, most theoretical models of the complex interaction between fluid and solid mechanics have used relatively simple 'tube laws' to describe the elastic behaviour of the tube wall. These tube laws relate the cross-sectional area of the tube to the local transmural pressure difference. The fluid flow was either modelled one-dimensionally or *ad hoc* assumptions about the shape of the deformed cross-sectional area had to be made (Wild *et al.* 1977). Membrane theory has been used to model axisymmetric deformations of the tube [e.g. Hart & Shi (1992) who modelled the axisymmetric deformation of semi-infinite tubes composed of sections of different materials], but these models cannot be used to investigate the postbuckling behaviour of the collapsed tube.

A typical experimental set-up is shown in Figure 1. Inside a pressure chamber, a finite-length collapsible tube is mounted on two rigid tubes and viscous fluid is pumped through. Various combinations of parameters can be varied in the experiments (e.g., external pressure and volume flux or external pressure and upstream pressure, etc.). For sufficiently large external pressure and/or volume flux, the tube collapses at the downstream end, i.e. it buckles nonaxisymmetrically [see, e.g., Elad *et al.* (1992)]. Since the collapsed region is very close to the mounting, end effects can be expected to play an important role but they cannot be captured by the tube laws mentioned above.

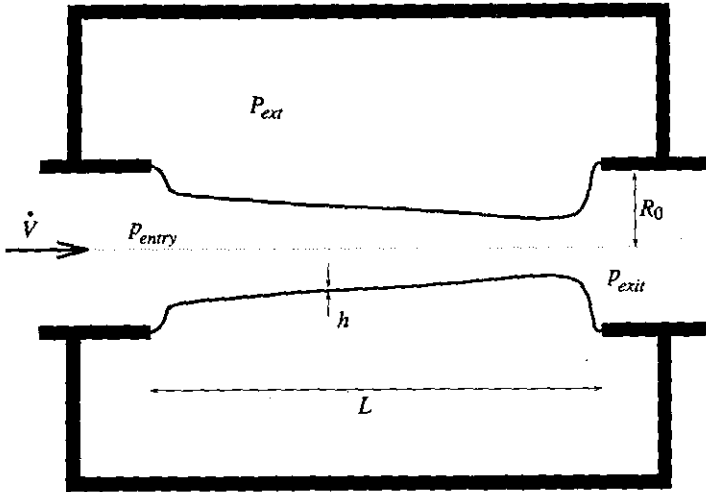In this paper we use Lagrangian nonlinear shell theory to develop an improved

Figure 1. Sketch of the model problem.

model of the elastic behaviour of the tube wall. In the first section the shell theory used is summarized briefly, but in the form needed to describe general nonaxisymmetric deformations. The fluid flow is modelled using lubrication theory. In this paper we examine the pre-buckling deformation, i.e. the case of steady flow and axisymmetric deformations. The influence of bending stiffness, which has not been taken into account in previous models, is examined. Also investigated are the effects of wall shear stress and axial pre-stretch of the tube. Diagrams of the pressure drop as a function of the volume flux under various conditions are presented. Finally, the exact nonlinear shell theory used in this paper is compared to Sanders' (1963) moderate rotation theory and an improvement to his theory is suggested.

2. THE MODEL

We model the tube of length, L, undeformed radius, R_0, and wall thickness, h, as a cylindrical shell and describe its deformation using a geometrically nonlinear Kirchhoff/Love type shell theory [e.g., Wempner (1973)]. Using the usual assumptions (thickness of the shell is constant, normals to the undeformed midplane remain normal), the deformation of the shell can be expressed in terms of the midplane displacement, $\mathbf{v}$. We use Lagrangian coordinates, x^α, (Greek and Latin indices have values 1, 2 and 1, 2, 3, respectively, and the summation convention is used) to parametrize the shell's midplane. Let $\mathbf{r}^0(x^\alpha)$ be the vector to a material point on the midplane before deformation. We choose cylindrical coordinates as the Lagrangian coordinates (x^1 and x^2 are the arc-lengths in the axial and circumferential direction, respectively). Lower case letters refer to the undeformed reference state and the superscript '0' indicates the vector to the midplane:

$$\mathbf{r}^0 = (x^1, R_0 \sin(x^2/R_0), R_0 \cos(x^2/R_0))^{\mathsf{T}}, \qquad x^1 \in [0, L], \qquad x^2 \in [0, 2\pi R_0]. \tag{1}$$

The position of an arbitrary point in the shell at a distance x^3 from the midplane can be written as (see Figure 2):

$$\mathbf{r} = \mathbf{r}^0 + x^3 \mathbf{n}, \qquad x^3 \in [-h/2, h/2]; \tag{2}$$

$\mathbf{n} = \mathbf{a}_3$ is the unit vector normal to the two midplane base vectors $\mathbf{a}_\alpha = \mathbf{r}^0_{,\alpha}$, where the
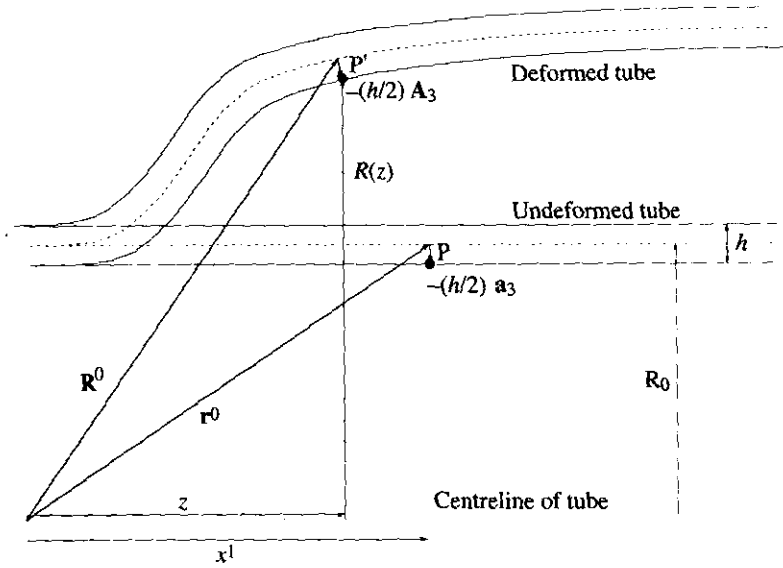
Figure 2. Transformation between Lagrangian coordinates used for the description of the tube wall and Eulerian fluid coordinates: the material point P on the inner surface of the undeformed tube wall is moved to P'.

comma denotes partial differentiation with respect to x^α. Let $a_{\alpha\beta} = \mathbf{a}_\alpha \cdot \mathbf{a}_\beta$ be the covariant metric tensor, a its determinant and $b_{\alpha\beta} = \mathbf{n} \cdot \mathbf{a}_{\alpha,\beta}$ the curvature tensor of the undeformed midplane. After deformation, the material point on the midplane with the Lagrangian coordinates x^α has been displaced to a new position $\mathbf{R}^0(x^\alpha) = \mathbf{r}^0(x^\alpha) + \mathbf{v}(x^\alpha)$. We decompose the displacement vector, $\mathbf{v}$, into the undeformed basis, $\mathbf{v} = v^j \mathbf{a}_j$. We use capital letters for the quantities associated with the deformed tube: base vectors, $\mathbf{A}_\alpha = \mathbf{R}^0_{,\alpha}$, unit normal, $\mathbf{N}$, metric tensor, $A_{\alpha\beta} = \mathbf{A}_\alpha \cdot \mathbf{A}_\beta$, curvature tensor, $B_{\alpha\beta} = \mathbf{N} \cdot \mathbf{A}_{\alpha,\beta}$ and vector to a point in the deformed shell, $\mathbf{R} = \mathbf{R}^0 + x^3 \mathbf{N}$. Then, the deformation is described by the strain tensor, $\gamma_{\alpha\beta} = 1/2(A_{\alpha\beta} - a_{\alpha\beta})$, and the bending tensor $\kappa_{\alpha\beta} = -(B_{\alpha\beta} - b_{\alpha\beta})$. In spite of the large deformations, the strain of the shell is still relatively small [Elad et al. (1992) report about 2–3% maximum extension in their experiments]; therefore, we use Hooke's law (linear constitutive equations) and Love's first approximation to express the strain energy function, ϕ (strain energy per unit area of the undeformed midplane of the shell) in terms of the strain and bending tensors:

$$\phi = \tfrac{1}{2} h E^{\alpha\beta\gamma\delta}(\gamma_{\alpha\beta}\gamma_{\gamma\delta} + \tfrac{1}{12}h^2\kappa_{\alpha\beta}\kappa_{\gamma\delta}), \tag{3}$$

with the plane stress stiffness tensor

$$E^{\alpha\beta\gamma\delta} = \frac{E}{2(1+v)}\left(a^{\alpha\gamma}a^{\beta\delta} + a^{\alpha\delta}a^{\beta\gamma} + \frac{2v}{1-v}a^{\alpha\beta}a^{\gamma\delta}\right), \tag{4}$$

where E is Young's modulus, v is Poisson's ratio and $a^{\alpha\beta}$ is the contravariant metric tensor of the undeformed midplane, $a^{\alpha\beta}a_{\beta\gamma} = \delta^\alpha_\gamma$.

We use the principle of virtual displacements

$$\int_0^{2\pi R_0} \int_0^L (\delta\phi - (\mathbf{f} \cdot \delta\mathbf{R})|_{x^3 = \pm h/2})\sqrt{a}\, dx^1\, dx^2 = 0, \tag{5}$$

where $\mathbf{f}$ is the load per unit area of the undeformed midplane acting on the shell surface.

We nondimensionalize the coordinates x^i, the displacements $\mathbf{v}$ and the bending tensor, $\kappa_{\alpha\beta}$, with the undeformed radius, $x^i = x^{*i}R_0$, $\mathbf{v} = \mathbf{v}^*R_0$, $\kappa_{\alpha\beta} = \kappa_{\alpha\beta}^*/R_0$ and the stiffness tensor and the loads with Young's modulus, $E^{\alpha\beta\gamma\delta} = E^{*\alpha\beta\gamma\delta}E$ and $\mathbf{f} = \mathbf{f}^*E$. The strain tensor, $\gamma_{\alpha\beta}$, is already dimensionless. Then we obtain the following variational equation for the equilibrium of the tube wall

$$\int_0^{2\pi} \int_0^{L/R_0} \left[E^{*\alpha\beta\gamma\delta}\left(\gamma_{\alpha\beta}\delta\gamma_{\gamma\delta} + \frac{1}{12}\left(\frac{h}{R_0}\right)^2 \kappa_{\alpha\beta}^*\delta\kappa_{\gamma\delta}^* \right) - \left(\frac{R_0}{h}\right)(\mathbf{f}^* \cdot \delta\mathbf{R}^*)|_{x^{*3}=\pm h/(2R_0)} \right]$$
$$\times \sqrt{a}\, dx^{*1}\, dx^{*2} = 0, \quad (6)$$

where the variations of strain and bending tensor have to be taken with respect to the displacements, v^{*i}, and their derivatives. The tube is clamped at both ends. Therefore, at $x^1 = 0$ and $x^1 = L$ the displacements have to be prescribed (which allows the possibility of pre-stretch) and we have $dv^3/dx^1 = 0$. This formulation is valid for arbitrary deformations, as long as the strains are small enough to justify the use of Hooke's law. This small strain assumption implies that the large deformation of the tube correspond to large rigid body rotations. Therefore, we used the exact, fully nonlinear expressions for the strain and bending tensors and did not introduce any further simplifications in the strain-displacement relations. Sanders (1963) developed a shell theory for small strains and moderately large rotations which has been widely used for similar problems. In Section 4.4 we shall show that Sanders's strain-displacement relations have to be slightly modified to obtain accurate results in the large displacement regime. In this paper we restrict ourselves to axisymmetric deformations ($v^2 = 0$, $\partial/\partial x^2 = 0$).

The elastic and fluid problem are coupled through wall position and through the traction exerted by the fluid on the tube wall. Assuming that the product of wall slope (α, say) and Reynolds number of the flow is small everywhere, $\mathrm{Re}\,\alpha \ll 1$, we can use lubrication theory to model the flow. We use Eulerian cylindrical coordinates (r^*R_0, z^*R_0, θ) for the fluid flow. In this coordinate system the position of the tube wall is given as $R_{tube}(z) = R_{tube}^*(z^*)R_0$. This can be translated into the Lagrangian description of the tube wall needed above by following the path of particles on the inner tube wall during deformation (Figure 2), so that

$$z = \left(\mathbf{R}^0 - \frac{h}{2}\mathbf{A}_3 \right) \cdot \mathbf{a}_1, \quad (7)$$

$$R_{tube}(z) = \sqrt{\left| \mathbf{R}^0 - \frac{h}{2}\mathbf{A}_3 \right|^2 - z^2}. \quad (8)$$

This transformation is valid for arbitrary deformations but for nonaxisymmetric deformations the vectors in Figure 2 do not necessarily lie in the same plane. For long thin tubes with $L \gg h$ we can neglect the effect of the rotation of the normal in this transformation and use

$$z \approx x^1 + v^1 \quad \text{and} \quad R_{tube} \approx R_0 - h/2 + v^3. \quad (9)$$

This introduces an error of order $\mathcal{O}(h/L)$ which is $\mathcal{O}(h/R)$ smaller than the error already introduced by using lubrication theory.

Lubrication theory for circular tubes with slowly varying cross-sectional area predicts a parabolic velocity profile

$$u_z(r, z) = \frac{2\dot{V}}{\pi R_{tube}^2(z)}\left[1 - \left(\frac{r}{R_{tube}(z)}\right)^2 \right], \quad (10)$$

where $\dot{V}$ is the volume flux through the tube. In order to find the traction exerted by the fluid on the wall we first have to determine the stress vector of the fluid at the wall. Then, it has to be decomposed into components normal and parallel to the deformed wall. Within the accuracy of lubrication theory, the stress component normal to the tube wall is equal to the fluid pressure, and the tangential component is equal to the wall shear stress, $\tau_w = \tau_{rz}$, due to the parabolic velocity profile.

The local pressure gradient is that of an infinitely long tube of the same cross-sectional area. If we nondimensionalize the pressure with Young's modulus, $p = p^*E$, we obtain

$$\frac{\partial p^*}{\partial z^*} = -\left(\frac{R_0}{L}\right)\frac{q}{[R^*_{tube}(z^*)]^4}, \tag{11}$$

where the parameter

$$q = \frac{8\mu\dot{V}L}{\pi R_0^4 E} \tag{12}$$

represents the nondimensional pressure drop through the undeformed tube. It increases linearly with the volume flux.

The nondimensional wall shear stress, $\tau_w^* = \tau_w/E$, due to the parabolic flow profile is:

$$\tau_w^* = \tau_{rz}^* = \frac{1}{2}\frac{R_0}{L}\frac{q}{[R^*_{tube}(z^*)]^3}. \tag{13}$$

3. NUMERICAL IMPLEMENTATION AND VALIDATION

Since a variational equation exists for the elastic part of the problem, a displacement-based finite element technique was chosen to discretize the equations. Carrying out the variations in (6) is a straightforward process but involves some lengthy algebra. We used the symbolic algebra manipulator REDUCE to express (6) in terms of the displacements and their derivatives. Equation (6) can thereby be written as

$$\int_0^{2\pi}\int_0^{L/R_0} (\varphi_i\delta v^i + \varphi_{i\alpha}\delta v^i_{,\alpha} + \varphi_{i\alpha\beta}\delta v^i_{,\alpha\beta})\sqrt{a}\,dx^{*1}\,dx^{*2} = 0. \tag{14}$$

The φ terms contain up to second derivatives of the displacements; therefore we need shape functions with continuous first derivatives across the element boundaries. We used isoparametric Hermite elements with nodal displacements and slopes as independent degrees of freedom (Bogner et al. 1967). For the one-dimensional axisymmetric case the displacement field within element E (with local coordinate $s \in [0, 1]$) depends only on x^{*1} and is interpolated as

$$v^{*i}(s) = \sum_{j,k=1}^{2} V^{iJ(j,E)k}\psi_{jk}(s), \tag{15}$$

with shape functions $\psi_{11} = 2s^3 - 3s^2 + 1$, $\psi_{12} = s^3 - 2s^2 + s$, $\psi_{21} = -(2s^3 - 3s^2)$ and $\psi_{22} = s^3 - s^2$; $J(j, E)$ is the global node number corresponding to the local node number j ($j = 1, 2$) in element number E. To generate isoparametric elements we used the same shape functions to map the local coordinate, s, to the global coordinate, x^{*1},

$$x^{*1}(s) = \sum_{j,k=1}^{2} X^{J(j,E)k}\psi_{jk}(s). \tag{16}$$

This mapping has to interpolate the x^{*1}-coordinates of the nodal points J, x_J^{*1}, therefore we have $X^{J1} = x_J^{*1}$. The Jacobian of the mapping, dx^{*1}/ds, can have any positive value, but it has to be continuous across element boundaries. This was achieved by choosing $X^{J2} = h_{min}$, where h_{min} is the size of the smaller of the two elements sharing node J.

We insert (15) into (14) and make use of the axisymmetry. The remaining integration over x^{*1} has to be split up into integrations over the local coordinate s and a summation over the N elements, i.e.

$$\sum_{E=1}^{N} \sum_{j,k=1}^{2} \left\{ \int_0^1 (\varphi_i \psi_{jk} + \varphi_{i1} \psi_{jk,1} + \varphi_{i11} \psi_{jk,11}) \sqrt{a} \frac{dx^{*1}}{ds} \, ds \right\} \delta V^{iJ(j,E)k} = 0. \qquad (17)$$

The variations of those V^{ijk} which are not determined by boundary conditions are arbitrary. This leads to the following set of nonlinear algebraic equations, f_{ijk}, for the unknown V^{ijk}:

$$f_{ijk} = \sum_{E=1}^{N} \int_0^1 \left\{ (\varphi_i \psi_{lk} + \varphi_{i1} \psi_{lk,1} + \varphi_{i11} \psi_{lk,11})|_{J(l,E)=j} \frac{dx^{*1}}{ds} \sqrt{a} \right\} ds = 0. \qquad (18)$$

We solved this set of equations with a Newton–Raphson technique, using the displacement variables, V^{ijk}, as the independent variables. The fluid flow was incorporated in the following way: at every stage of the iteration the current values of the V^{ijk} determine the shape of the tube wall. We specify the volume flux and the pressure of the fluid as it enters (or leaves) the collapsible segment, $p|_{x^1=0} = p_{entry}$ (or $p|_{x^1=L} = p_{exit}$). Then we use (11) to determine the pressure distribution in Lagrangian coordinates [by using (9) we see that $d/dz = 1/(1 + v_{,1}^1) \, d/dx^1$; use of (7) makes the Jacobian of this transformation more complicated but the effect on the result is negligible]. Equation (13) gives the tangential load on the tube wall. The load terms in (6) can therefore be determined and the residuals of the functions f_{ijk} can be evaluated. Then this information is used to update the values of the unknowns using the Newton–Raphson technique. The Jacobian matrix

$$J_{(i,j,k)(I,J,K)} = \frac{\partial f_{ijk}}{\partial V^{IJK}} \qquad (19)$$

was determined using finite differencing. A finite difference step of $\Delta V^{ijk} = 10^{-4}$ was found to be optimal. The integrations in (18) were carried out numerically with three Gauss points per element. Hence, the integrand of (18) only needs to be evaluated at the Gauss points within each element (squares in Figure 3). We used a numerical three-point Gauss–Radau integration [see, e.g., Kopal (1955)] to integrate the pressure gradient from one FEM Gauss point to the next one. The integration points for the numerical integration of the pressure gradient are marked with solid black circles in Figure 3. The results were not changed by an increase in the number of integration points in either of these numerical integrations.

The code was developed on a Silicon Graphics 4D/480 computer with four processors and it was specifically designed for parallel processing. The most important feature of the implementation is the determination of the elements of the Jacobian matrix in parallel mode (CPU time reduced to about 35% of that of the serial version when running on four processors).

It should be noted that the fluid–solid interaction leads to a nonsymmetric and dense Jacobian matrix. This can easily be seen from the following argument: instead of using the variational principle (14), the system of equations (18) could have been derived by
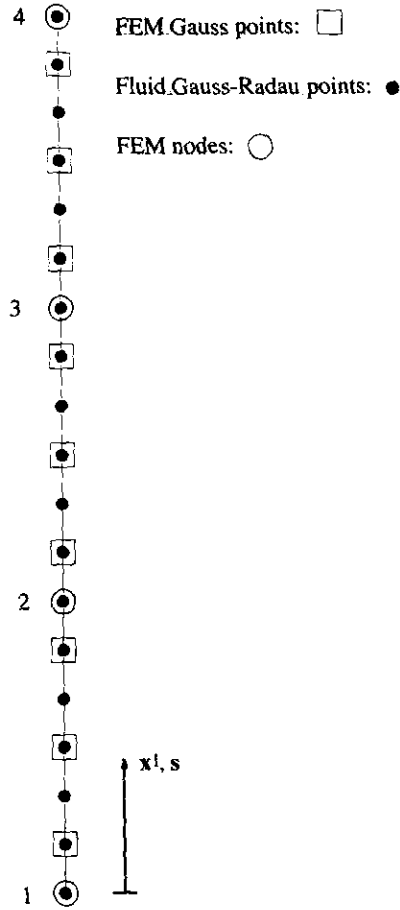
Figure 3. Integration scheme for coupled fluid-solid solver. The integrand in (18) needs to be evaluated at the three FEM Gauss points within each element. The fluid pressure is determined by integrating (11) numerically using a three point Gauss–Radau rule.

an examination of the local balance of internal and external forces. In this sense, the functions f_{ijk} are a measure of the imbalance between the generalized internal and external forces associated with the generalized displacements, V^{ijk}. Therefore, the coefficient $J_{(i,j,k)(I,J,K)}$ represents the change in the force imbalance, f_{ijk}, due to a small change in the generalized displacement, V^{IJK}.

Without fluid flow, the change in one of the discrete generalized displacements, V^{ijk}, only affects the balance of forces in the two adjacent elements. This is due to the particular choice of shape functions in the FE method. Their finite support leads to a sparse band structure of the Jacobian matrix. In this case the Jacobian matrix is also symmetric and positive definite, as can be deduced from the conservation of energy (the elastic system alone is conservative).

To examine the case with through flow let us assume that the pressure at the upstream end of the tube is prescribed. Then the pressure distribution is obtained by integrating the pressure gradient (11) in the downstream direction. This implies that changes in the discrete displacements at one point affect the pressure distribution (and therefore the local balance of forces) everywhere downstream of this point, whereas the pressure upstream of this point remains unaffected. This mechanism couples upstream and downstream degrees of freedom and leads to an asymmetric and rather

dense Jacobian matrix. Physically, the asymmetry corresponds to the fact that the elastic system can now gain energy from the fluid flow.

The asymmetry of the Jacobian matrix increases the computational cost considerably. Firstly, a substantially larger number of entries in the Jacobian matrix has to be computed. Secondly, the linear system to be solved during the Newton–Raphson iteration has to be solved using LU decomposition. This is much slower than the banded Cholesky solver which can be used for the symmetric positive definite matrix of the no-flow case.

For a typical FEM discretization of 50 elements, the CPU time required to compute a converged solution increases from about 17 s for the no-flow case to about 120 s for the case with through flow.

To validate the results of the numerical computations, we carried out a number of tests. Firstly, we checked that for small displacements the FEM code yields the same results as the analytical solution of the linearized equations [see, e.g., Schnell & Eschenauer (1984)]. Secondly, we compared our exact (within the framework of the Kirchhoff–Love assumption and the linear constitutive equations) equations to Sanders' moderate rotation theory (Sanders 1963). As will be shown in Section 4.4, Sanders' equations have to be modified slightly to yield accurate results for the large displacement regime. Replacing the exact expressions for strain and bending tensor and their variations in our code by the modified Sanders expressions, as derived below, had very little effect on the results. The modified Sanders' equations are much simpler than the exact ones. For the no-flow case we could transform them into a system of six first-order ODEs which we solved using the finite difference solver D02GAF from the NAG library. The results were in perfect agreement with those obtained using our FEM code. We also compared our results for this load case with the results obtained using the commercial FEM package ABAQUS. We found good agreement with our results.

Finally, we tested the numerical integration of the pressure gradient by prescribing a wall shape for which (11) could be integrated analytically and compared the results of the numerical and analytical integration. The integration scheme described above was found to be sufficiently accurate. Different numbers of elements were used to check for convergence.

4. RESULTS AND DISCUSSION

The different mechanisms involved in the interaction between fluid and solid mechanics are examined in three steps. First, to illustrate the general deformation characteristics of the tube we investigate the deformation of the tube without any through flow. The effects of the pressure distribution due to the viscous flow can then be explained easily, and in the last step we include the effect of the wall shear stress. Then, the effect of axial pre-stretch is examined and plots of the tube resistance as a function of the volume flux are presented. Finally, possible simplifications of the shell equations are discussed.

The computations presented here were carried out with $L/R_0 = 10$, $h/R_0 = 1/20$ and $\nu = 0.49$. This corresponds to a nondimensional bending stiffness of

$$K = \frac{1}{12(1 - \nu)^2} \left(\frac{h}{R_0}\right)^3 = 1.37 \times 10^{-5}. \tag{20}$$

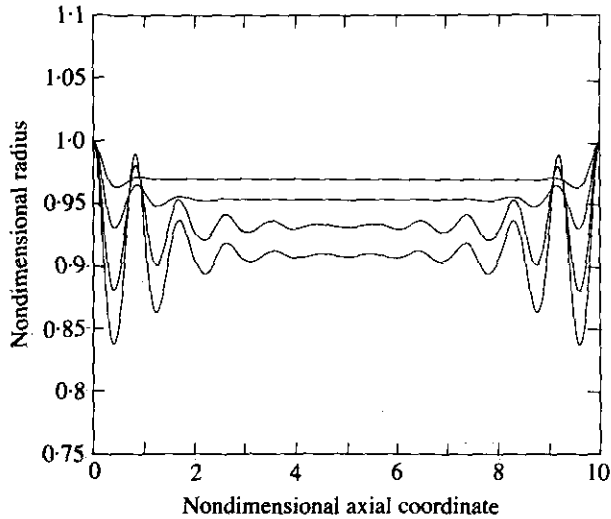Poisson's ratio and relative wall thickness were chosen to be in the range of

Figure 4. Deformation of the tube without through flow $p^*_{ext} = 0$, constant fluid pressure, $p^* = -2 \cdot 0 \times 10^{-3}$ to $-5 \cdot 0 \times 10^{-3}$ in equal steps.

parameters in the experiments of Elad *et al.* 1992, where (by the standards of shell theory) relatively thick-walled rubber tubes had been used. We used a smaller L/R_0 ratio to enhance the interesting effects. The effect of a change of tube geometry is discussed in the last section.

4.1. DEFORMATION OF AN UNSTRETCHED TUBE

In the absence of fluid flow, a stepwise increase in external pressure gives rise to the deformation shown in Figure 4. For small external pressures the deformation is that predicted by linear shell theory [see, e.g., Schnell & Eschenauer (1984)]: a very rapidly damped wave-like deformation pattern of the form $v^{*3} \sim \exp[\pm(1 \pm i)\rho x^{*1}]$ with

$$\rho \approx \sqrt[4]{3(1 - v^2)}\sqrt{\frac{R_0}{h}} \gg 1 \tag{21}$$

gives rise to a sharp bending boundary layer near the mounting (the horizontal slope at the mounting can hardly be resolved in the plots). Away from the mounting, the radius is nearly constant and equal to the value predicted by membrane theory. As the load increases, the wave-like pattern grows both in amplitude and axial extension as the geometrical nonlinearities play an increasingly important role (see the Appendix for a discussion of this peculiar wavy deformation pattern).

Figure 5 shows the effect of an increase in the volume flux when only the traction normal to the tube wall is taken into account. The external pressure and the upstream pressure, p_{entry}, are set to a constant value while the volume flux is increased in equal steps.

The viscous pressure drop increases with the volume flux—see equation (11); therefore, the compressive load and the deformation increase in the downstream direction. Since the reduced cross-sectional area increases the pressure drop even further, see (11), the collapse at the downstream end is accelerated. As the deformation of the tube grows at the downstream end, the wave-like pattern discussed above begins to develop and grows in the upstream direction. This pattern also
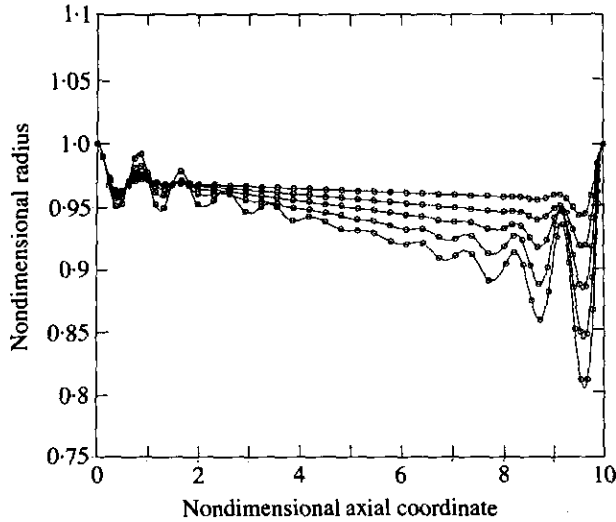
Figure 5. Deformation with through flow, only traction normal to tube wall taken into account, $p_{ext}^* = 0$, $p_{entry}^* = -2 \cdot 0 \times 10^{-3}$, dimensionless volume flux, $q = 6 \cdot 0 \times 10^{-4}$ to $30 \cdot 0 \times 10^{-4}$ in equal steps.

dominates the pressure gradient since $dp/dz \sim R_{tube}^{-4}$. As the pressure distribution itself is obtained by an integration, it is much smoother and the wavy pattern is nearly averaged out.

The dominating displacement of the tube is radially inwards (markers identify the position of material points of the tube wall).

When the wall shear stress is taken into account, the deformation pattern changes significantly, as shown in Figure 6. The general effect of the wall shear stress is to move the wall downstream. Since no displacements are possible at the downstream end, the tube starts to 'fold up' and increases the amplitude of the wave-like pattern which is induced by the essentially unchanged pressure distribution.

As can be seen in (13) we have $\tau_w \sim R_{tube}^{-3}$, therefore τ_w is significantly higher in the narrower cross-sections of the tube. As a result of this, material points (again indicated
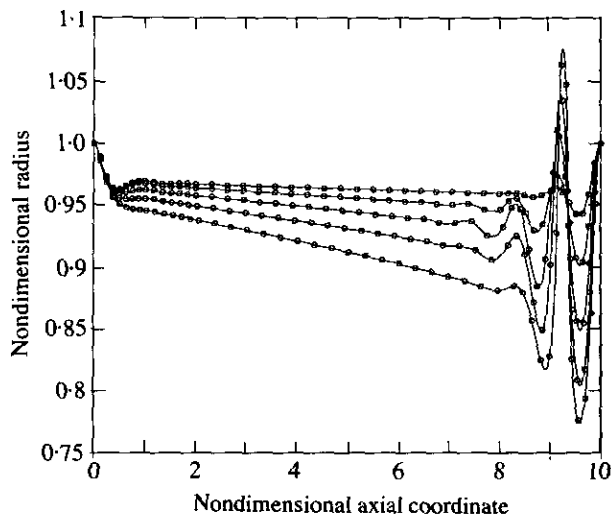

Figure 6. Deformation with through flow, wall shear stress included. $p_{ext}^* = 0$, $p_{entry}^* = -2 \cdot 0 \times 10^{-3}$, dimensionless volume flux, $q = 6 \cdot 0 \times 10^{-4}$ to $30 \cdot 0 \times 10^{-4}$ in equal steps.
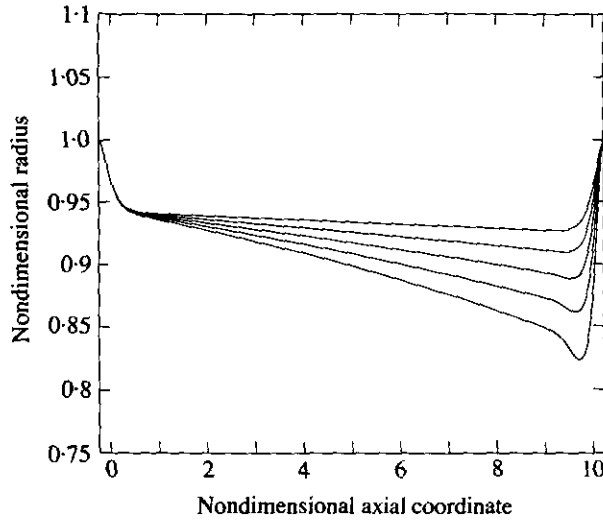
Figure 7. Deformation with 5% axial pre-stretch. $p^*_{ext} = 0$, $p^*_{entry} = -2 \cdot 0 \times 10^{-3}$, dimensionless volume flux, $q = 6 \cdot 0 \times 10^{-4}$ to $30 \cdot 0 \times 10^{-4}$ in equal steps.

by markers) are displaced in the downstream direction while the wave pattern itself remains nearly stationary.

4.2. EFFECT OF AXIAL PRE-STRETCH

Since veins and arteries in the human body are under pre-tension [they contract by up to 40% when they are cut; see Bergel (1972)], experiments have been carried out with axially pre-stretched tubes. The effects of axial pre-stretch can be examined with this model by prescribing nonzero axial displacements of the tube at the upstream and downstream ends. In this case, two effects compete with each other. Firstly, the pre-tension tends to make the tube stiffer. However, the axial pre-stretch in combination with the cylindrical geometry of the tube also increases the radial contraction of the tube due to the Poisson effect. Therefore, for a given external pressure, the cross-sectional area of a pre-stretched tube is smaller than that of an unstretched tube. This results in an increased pressure drop in the fluid which increases the compressive load on the tube. The combination of these two effects can be seen in Figure 7. The radial deformation of a pre-stretched tube is greater than that of an unstretched one but the increased axial tension suppresses the oscillations of the tube near the downstream end.

To explain the latter effect, let us examine small deformations superimposed on a pre-stretched tube whose length has been changed from L to $L + U$. To simplify the analysis we assume that a uniform pressure,

$$p^*_0 = \left(\frac{h}{R_0}\right)\frac{\nu\epsilon_U(\epsilon_U + 2)}{2(1 - \nu^2)[1 - (h/2R_0)](1 + \epsilon_U)}, \tag{22}$$

acts on the inside of the tube. The relative pre-stretch is denoted by $\epsilon_U = U/L$. If the external pressure is zero, p^*_0 suppresses the contraction due to the Poisson effect and the pre-stretched displacement field is

$$v^{*1} = v^{*1}_0 = \left(x^{*1} - \frac{L}{2R_0}\right)\frac{U}{L} \quad \text{and} \quad v^{*3} = v^{*3}_0 = 0. \tag{23}$$

The governing differential equations for the displacements are the Euler–Lagrange equations of the variational equation (6). Inserting the displacements $v^{*1} = v_0^{*1} + u$ and $v^{*3} = v_0^{*3} + w$ and linearizing with respect to $u, w \gg 1$ we obtain two coupled linear ODEs which govern the small deformations superimposed on the pre-stretched state. If no tangential load acts on the tube, we can eliminate u from the equation for w and obtain the following ODE for the nondimensional radial displacement, w:

$$kw'''' + m_1 w'' + m_2 w = \frac{p_1^*}{[1 - (h/2R_0)](1 + \epsilon_U)} + C; \tag{24}$$

p_1^* is the small pressure superimposed on the constant initial pressure, p_0^*, and C is a constant of integration, to be determined by the boundary conditions for u. Primes denote differentiation with respect to x^{*1}. The coefficients are:

$$k = \frac{1}{12(1 - v^2)} \left(\frac{h}{R_0}\right)^3, \tag{25}$$

$$m_1 = -\frac{3\epsilon_U^2 + 6\epsilon_U + v(h/R_0)^2}{6(1 - v^2)} \left(\frac{h}{R_0}\right), \tag{26}$$

$$m_2 = \frac{(h/R_0)}{(1 - v^2)(3\epsilon_U^2 + 6\epsilon_U + 2)} \left\{ v\epsilon_U^3(\tfrac{3}{2}\epsilon_U + 6) + 2(1 - v^2) + \frac{1}{6}\left(\frac{h}{R_0}\right)^2 \right.$$

$$\left. + \epsilon_U \left[\epsilon_U \left(3 + \frac{1}{4}\left(\frac{h}{R_0}\right)^2 + v(7 - 2v)\right) + 6 + \frac{1}{2}\left(\frac{h}{R_0}\right)^2 + v(2 - 4v) \right] \right\}. \tag{27}$$

The homogeneous solution of (24) is of the form $w \sim \exp(\lambda x^{*1})$ with four roots, $\lambda = \pm\alpha \pm i\beta$. For small pre-stretch, the influence of m_1 on the value of the roots is negligible and we have $\alpha, \beta > 0$ which yields the strongly damped wave pattern shown in Figure 4. As the pre-stretch increases, the imaginary part β—and with it the oscillatory component in the solution—decreases while the ratio m_1/m_2 increases. If ϵ_U is greater than a certain value $\bar{\epsilon}_U$, we have $m_1^2 > 4m_2$ which yields four real roots and the oscillatory component vanishes (see Figure 8). Figure 9 shows the left end of a tube subject to a small constant load, p_1^*, for various values of the pre-stretch. As the pre-stretch increases, the characteristic bump at the end of the bending boundary layer begins to disappear.

Analysing the physical origin of the coefficients in (24) allows the following
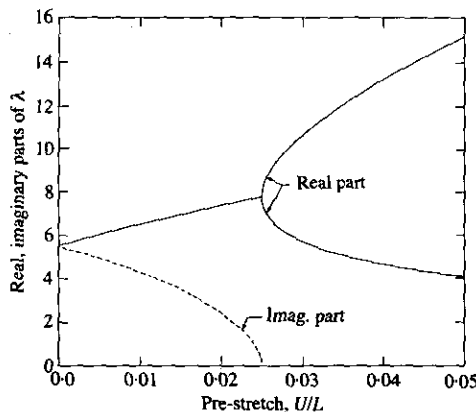

Figure 8. Real and imaginary part of the roots $\lambda = \pm\alpha \pm i\beta$. The imaginary part decreases with increasing pre-stretch and vanishes for $U/L > \bar{\epsilon}_U$ ($\bar{\epsilon}_U \approx 2\cdot50\%$ for the geometry used).
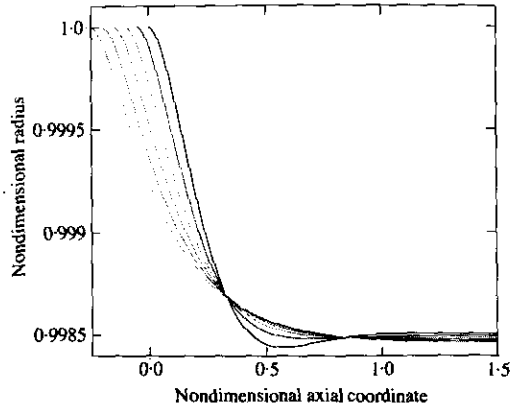
Figure 9. Left end of the pre-stretched tube with $U/L = 0\%, 1\%, \ldots, 5\%$ under $p_{ext}^* = 0$ and superimposed internal pressure, $p_i^* = -1\cdot 0 \times 10^{-4}$.

interpretation of this change in the deformation characteristic: for small pre-stretch, the tube deformation is governed by the interaction between bending moments and circumferential membranes stresses [which give rise to the coefficients k and m_2, respectively—see any derivation of the equations without pre-stretch based on the balance of internal forces; e.g., Schnell & Eschenauer (1984)]. The axial pre-stretch generates axial membrane forces which give rise to a w'' term as in the equation of an elastic string.

Therefore, the change in the deformation characteristic can be associated with the ratio of axial and circumferential membrane forces. Numerical studies indicate that this correlation holds, even in the finite displacement regime. In Figure 7 the finite pre-stretch together with moderate compressive forces yields a smooth displacement field due to the large axial membrane forces. As the volume flux increases, the radius at the downstream end is reduced. The resulting increase in circumferential membrane forces gives rise to the wavy deformation pattern which was initially suppressed by the dominating axial membrane forces.

4.3. RESISTANCE OF THE COLLAPSIBLE TUBE

The pressure drop through the collapsible tube depends on varios parameters. Apart from the geometrical parameters, h/R_0, L/R_0 and the axial pre-stretch of the tube, it is influenced by volume flux, transmural pressure difference at a fixed point and the position of this point. We examine the tube resistance for prescribed transmural pressure at either the upstream or the downstream end of the collapsible segment. These cases correspond to two different experimental set-ups.

Prescribing the volume flux and the transmural pressure at the upstream end of the collapsible segment could be realized experimentally by feeding the upstream end from a reservoir while connecting the downstream end to a volumetric pump. The relationship between pressure drop and volume flux for this case is shown in Figure 10. For a rigid tube, an increase in volume flux results in a proportional increase in the pressure drop. If the tube is flexible, the reduced downstream pressure increases its deformation and the reduced cross-sectional area enhances the pressure drop even further. In extreme cases, where the tube is allowed to buckle and collapse completely, the process results, experimentally, in 'flow limitation', where the volume flux cannot be increased above a maximum value. If the tube is pre-stretched, its cross-sectional
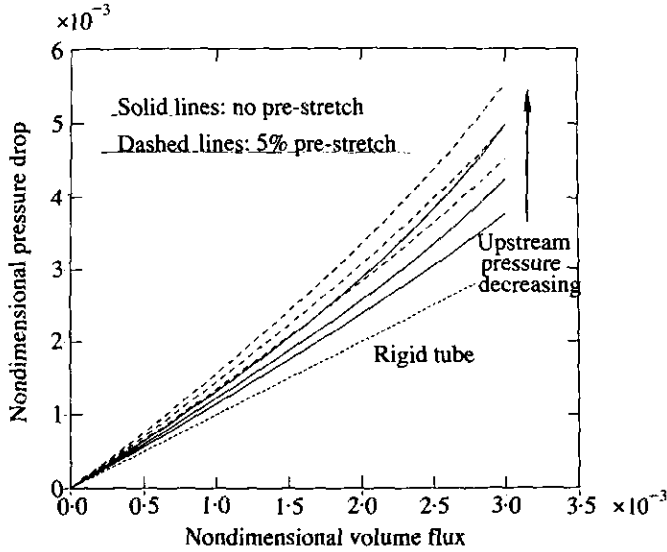
Figure 10. Resistance $p^*_{entry} - p^*_{exit}$ as a function of the nondimensional volume flux q for $p^*_{ext} = 0$. The upstream pressure, p^*_{entry}, is kept constant along the curves ($p^*_{entry} = 0 \cdot 0$, $-1 \cdot 0 \times 10^{-3}$ and $-2 \cdot 0 \times 10^{-3}$).

area is smaller than that of an unstretched tube under the same external pressure, and the pressure drop is correspondingly greater.

If the pressure at the downstream end were to be prescribed in the experiments, this end could be connected to a short rigid tube from which the fluid leaves under atmospheric pressure. Again, the volume flux could be prescribed by a volumetric pump, now at the upstream end of the collapsible segment. Figure 11 shows the deformation of the tube under these conditions. An increase in volume flux now increases the upstream pressure and the tube begins to bulge outwards (after overcoming the external pressure). This increase in cross-sectional area reduces the pressure drop and, if a sufficient length of the tube is bulged outwards, the resistance
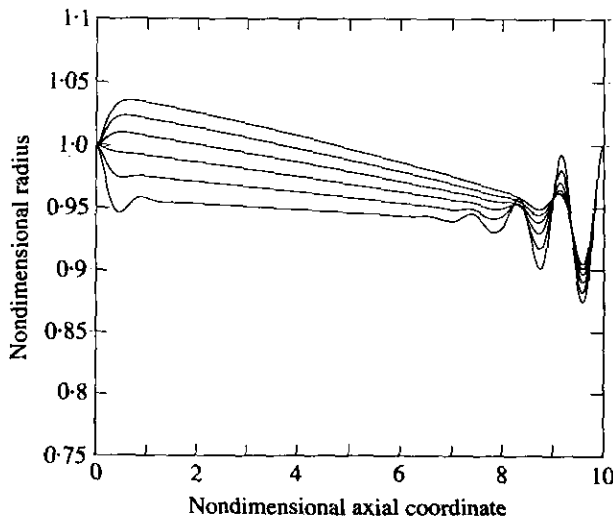

Figure 11. Deformation for prescribed pressure at downstream end. $p^*_{ext} = 0$, $p^*_{exit} = -2 \cdot 0 \times 10^{-3}$, dimensionless volume flux, $q = 1 \cdot 0 \times 10^{-3}$ to $6 \cdot 0 \times 10^{-3}$ in equal steps.
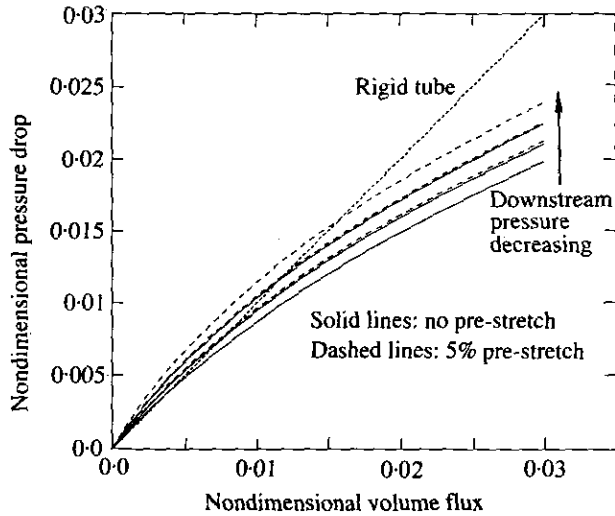
Figure 12. Resistance, $p^*_{entry} - p^*_{exit}$ as a function of the nondimensional volume flux, q for $p^*_{exit} = 0$. The downstream pressure, p^*_{exit} is kept constant along the curves ($p^*_{exit} = 0{\cdot}0$, $-2{\cdot}0 \times 10^{-3}$ and $-4{\cdot}0 \times 10^{-3}$).

becomes less than that of a rigid tube (Figure 12). Again, axial pre-stretch of the tube increases the pressure drop due to the reduced cross-sectional area. The predicted trend is also seen experimentally (Kamm & Pedley 1989).

Changing the geometry of the tube affects the deformation in the following way: reducing the relative thickness of the tube, h/R_0, reduces not only its stiffness but also the wavelength of the wave pattern according to (21). The absolute size of the bending boundary layer (or, equivalently, the wavelength of the wave pattern) is not affected by changes in L/R_0. However, for a given volume flux the pressure drop increases with L and the deformation is correspondingly greater.

4.4. COMPARISON WITH SANDERS' MODERATE ROTATION THEORY

As mentioned above, the small strain assumption implies that large deformations correspond to large rigid body rotations. This led us to use the exact expressions for the strain and bending tensor which leads to very complicated equations. The complexity of these equations is not too problematic for the numerical solution with the FEM code. Various simplifications of the exact equations have been derived by a number of authors and we shall now examine the validity of one particularly popular simplified theory.

Sanders (1963) derived a set of first-order nonlinear shell equations, based on the assumption of small strains and moderately large rotations. His equations are widely used for the stability analysis of shells and they have been used as the theoretical basis for shell elements in a number of commercial FEM packages. Sanders' equations are valid under the assumption that the midplane strains, $\gamma_{\alpha\beta}$, are $\mathcal{O}(\epsilon^2)$ and the rotations are $\mathcal{O}(\epsilon)$ where $\epsilon \ll 1$. Applying these equations to the axisymmetric deformation of cylindrical shells gives the following approximations for the determinant of the midplane metric tensor:

$$A = a + \mathcal{O}(\epsilon^2) = 1 + \mathcal{O}(\epsilon^2), \tag{28}$$

for the strain tensor $\gamma_{\alpha\beta} = \gamma^s_{\alpha\beta} + \mathcal{O}(\epsilon^3)$, with

$$\gamma^s_{11} = u' + \tfrac{1}{2}(w')^2, \qquad \gamma^s_{12} = \gamma^s_{21} = 0, \qquad \gamma^s_{22} = w, \tag{29}$$

and for the bending tensor, $\kappa_{\alpha\beta} = \kappa_{\alpha\beta}^s + \mathcal{O}(\epsilon^2)$, with

$$\kappa_{11}^s = -w'', \qquad \kappa_{12}^s = \kappa_{21}^s = \kappa_{22}^s = 0. \tag{30}$$

The exact expressions are

$$A = (1 + w)^2[(1 + u')^2 + (w')^2], \tag{31}$$

$$\gamma_{11} = u' + \tfrac{1}{2}(u')^2 + \tfrac{1}{2}(w')^2, \qquad \gamma_{12} = \gamma_{21} = 0, \qquad \gamma_{22} = w + \tfrac{1}{2}w^2, \quad \text{(32a,b,c)}$$

and

$$\kappa_{11} = \{-[(u' + 1)w'' - u''w'](w + 1)\}/\sqrt{A}, \tag{33}$$

$$\kappa_{12} = \kappa_{21} = 0, \qquad \kappa_{22} = (u' + 1)(w + 1)^2/\sqrt{A} - 1. \tag{34}$$

The most important feature of Sanders' approximation is the linearization of the components of the bending tensor, which simplifies the equations considerably. In fact, in this approximation only the axial strain component, γ_{11}, is nonlinear in the displacements. Furthermore, equation (28) allows us to calculate the equivalent external forces (projected onto the midplane of the deformed shell) under the assumption that the area elements of the deformed and the undeformed tube are equal,

$$\sqrt{A}\, dx^1\, dx^2 \approx \sqrt{a}\, dx^1\, dx^2 = dx^1\, dx^2. \tag{35}$$

To examine the validity of these approximations, we compared the results obtained using Sanders' expressions (dash-dot line in Figure 13) to the ones obtained using the exact ones (solid line in Figure 13). In Sanders' solution the wavy deformation pattern is less pronounced and the displacements are slightly smaller.

A careful analysis of the individual terms in Sanders' approximation shows that this discrepancy is caused by the following two effects: firstly, for a compressive deformation, Sanders' linearization of the circumferential strain component overestimates γ_{22} slightly. This makes the central section of the tube (whose deformation is governed by membrane stresses) slightly stiffer. We explained in the last section how the interaction of circumferential membrane stresses with the axial bending moments produces the
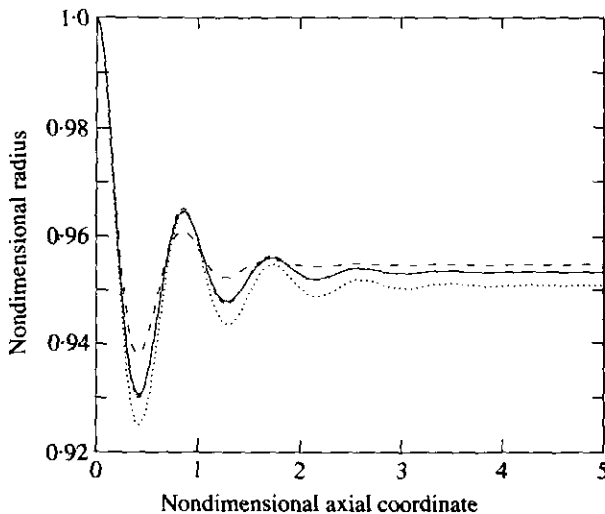

Figure 13. Comparison of Sanders' first order nonlinear theory with various corrections and exact theory for constant external pressure ($p^* = -3 \cdot 0 \times 10^{-3}$). Only the left half of the tube is shown. Solid line: exact theory; dash-dotted line: Sanders' theory; dotted line: modified Sanders theory with nonlinear γ_{22} and constant area assumption; dashed line: modified Sanders theory with nonlinear γ_{22} and exact change in area.

wavy deformation pattern. Therefore, it should not be surprising that the wave pattern is also slightly changed by an error in γ_{22}.

Secondly, in Sanders' approximation the equivalent external forces, calculated under the assumption of an unchanged determinant of the midplane metric tensor, are overestimated (the area on which the external pressure acts is reduced by a compressive deformation). In the large deformation regime investigated here, this effect cannot be neglected.

These two points suggest the following slight modifications to Sanders' theory: we retain the nonlinear expression (32c) for the circumferential strain component and calculate the equivalent external forces acting on the midplane of the deformed shell with the deformed metric tensor. This modification conserves the most essential feature of Sanders' theory (linear bending tensor) while it improves the accuracy of the solution remarkably. In Figure 13 the dashed line shows the solution calculated with the modified Sanders theory. It differs only very slightly from the solution obtained using the exact expressions. The dotted line is the deformation obtained by using the nonlinear expression for γ_{22} while neglecting changes in the tube area: the correct membrane stiffness and the overestimated compressive load lead to a larger deformation.

5. CONCLUSIONS

The axisymmetric deformation of a finite length collapsible tube has been modelled using geometrically nonlinear shell theory and lubrication theory. The mechanisms giving rise to the pre-buckling deformations in two different experimental set-ups with and without axial pre-stretch have been analysed and the dependence of the tube resistance on various parameters has been examined. The exact nonlinear shell theory has been compared to Sanders' moderate rotation theory. We have suggested two slight modifications to Sanders' equations which improve the accuracy of his theory significantly while they conserve its simplicity.

The inclusion of the tube bending stiffness allowed us to make accurate predictions of the tube pre-buckling deformation near the mounting where the nonaxisymmetric collapse begins in practise. On the basis of these results, a stability analysis to derive criteria for the beginning of this collapse is currently under way. Furthermore, the FEM code is being extended to two dimensions to examine the postbuckling deformations.

The following points should be noted regarding the assumptions made in the model: the Reynolds number does not explicitly enter our model since we nondimensionalized all pressures with Young's modulus, E. The fluid and wall properties only appear as the ratio of Young's modulus, E, and the typical fluid shear stress, $\mu \dot{V}/(\pi R_0^3)$. To check the condition Re $\alpha \ll 1$ we have to specify the tube material. The wall slope can be of considerable magnitude in the bending boundary layer which makes the use of lubrication theory questionable in these regions. To allow for arbitrary wall slopes and realistic Reynolds numbers, a solution of the Navier–Stokes equations should be used at some later stage to improve the model in this respect. In this context, it is interesting to note that Lowe & Pedley (1995) investigated the flow through a two-dimensional channel with a collapsible wall segment (modelled as an elastic membrane). They found surprisingly good agreement between lubrication theory and Stokes flow, even for strongly collapsed channels.

We have carried out calculations up to a range in which the real tube would buckle nonaxisymmetrically. This collapse would increase the pressure drop drastically.

Therefore, the values for the resistance shown in Figures 10 and 12 are lower than those measured in actual experiments [see, e.g., Bonis & Ribreau (1978)]. The tube shown in figure 8 in Elad *et al.* (1984), for geometrical parameters $h/R_0 = 0.06$; $L/R_0 = 35$ shows strong nonaxisymmetric collapse under a dimensionless transmural pressure difference of $p_{tm}^* = -6.56 \times 10^{-5}$ and a dimensionless volume flux, $q = 8.05 \times 10^{-7}$.

ACKNOWLEDGEMENTS

REFERENCES

BERGEL, D. H. 1972 The properties of blood vessels. In *Biomechanics. Its Foundations and Objectives.* (eds Y. C. Fung, N. Perrone, & M. Anliker) New Jersey: Prentice-Hall.

BOGNER, F. K., FOX, R. L. & SCHMIT, L. A. 1967 A cylindrical shell discrete element. *AIAA Journal* **5**, 745–750.

BONIS, M. & RIBREAU, C. 1978 Etude de quelques proprietés de l'écoulement dans une conduite collabable. *La Houille Blanche* **3/4**, 165–173.

ELAD, D., SAHAR, M., AVIDOR, J. M. & EINAV, S. 1992 Steady flow through collapsible tubes: measurements of flow and geometry. *ASME Journal of Biomechanical Engineering* **114**, 84–91.

HART, V. G. & SHI, J. Y. 1992 Joined dissimilar elastic thin tubes containing steady viscous flow. *Journal of Mechanics and Physics of Solids* **40**, 1507–1527.

KAMM, R. D. & PEDLEY, T. J. 1989 Flow in collapsible tubes: a brief review. *ASME Journal of Biomechanical Engineering* **111**, 177–179.

KOPAL, Z. 1955 *Numerical Analysis.* London: Chapman & Hall.

LOWE, T. W. & PEDLEY, T. J. 1995 Computation of Stokes flow in a channel with a collapsible segment. *Journal of Fluids and Structures* (under review).

SANDERS, J. L. 1963 Nonlinear theories for thin shells. *Quarterly Journal of Applied Mathematics* **21**, 21–36.

SCHNELL, W. & ESCHENAUER, H. 1984 *Elastizitätstheorie II: Schalen.* Mannheim, Vienna, Zürich: Bibliographisches Institut.

WEMPNER, G. 1973 *Mechanics of Solids.* New York: McGraw-Hill.

WILD, R., PEDLEY, T. J. & RILEY, D. S. 1977 Viscous flow in collapsible tubes of slowly-varying elliptical cross-section. *Journal of Fluid Mechanics* **81**, 273–294.

APPENDIX: THE MECHANISM FOR THE WAVY DEFORMATION

In this appendix we will illustrate the mechanism which gives rise to the wavy deformation of the cylindrical shell near the supports. As mentioned in the foregoing, the wavy deformation pattern is already present in the small displacement solution although its amplitude decays rapidly with increasing distance from the support. If the shell were not supported, then its deformation under uniform pressure would be homogeneous and equal to the value predicted by membrane theory. For small deformations, the presence of the supports is only felt in the narrow bending boundary layer near the ends of the shell. The most surprising feature of this bending boundary layer is
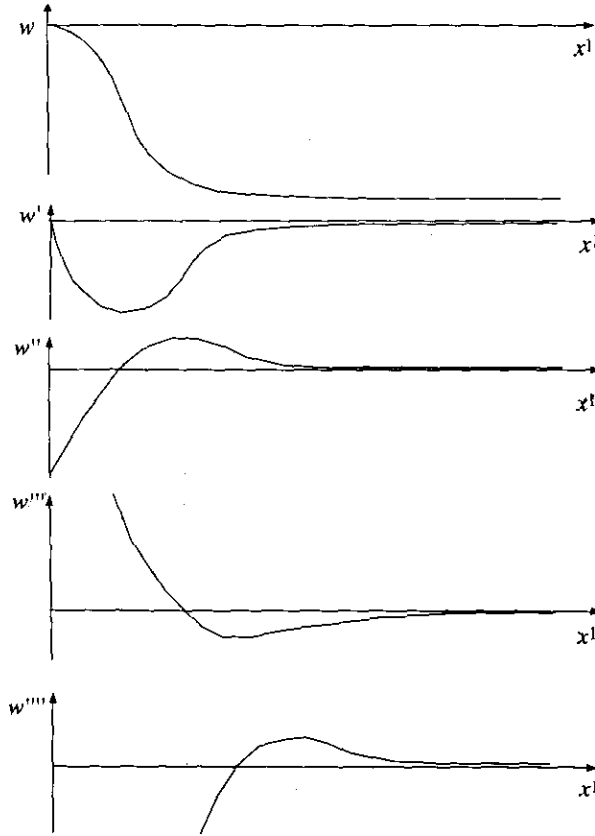
Figure 14. Sketch showing the first four derivatives of an assumed deformation in the bending boundary layer.

the appearance of the little bump in which the deformation is *larger* than in the central part of the shell, whereas, intuitively, one would expect a deformation similar to that shown in Figure 14.

As shown in Section 4.2, the small deformation of a cylindrical shell under constant external pressure is governed by an equation of the form

$$kw'''' + m_1 w'' + m_2 w = p = \text{const.,} \tag{A1}$$

where the w'' term does not play an important role as long as the pre-stretch is small.

Figure 14 shows a sketch of the first four derivatives of the assumed radial displacement w. Far away from the support, the displacement approaches a constant value and all derivatives vanish. Without the bump, the displacement, w, has a point of inflection (marked by the leftmost dashed line) before w begins to approach the value prescribed by the membrane forces. This point of inflection generates an extremum in the first derivative w', which leads to a point of inflection in w' further away from the support. This process repeats itself with evey new differentiation, and extremum and point of inflection move further and further into the shell. Now the governing ODE, equation (A1), requires that the sum of first, second and fourth derivatives be equal to a constant. From the sketch it is clear that the bump in the fourth derivative can only be balanced by a corresponding small bump in the displacement w itself.

Now the argument can be repeated and applied to the zone to the right of the bump in w: the zone between the bump and the region far away from the support contains a point of inflection. However, all slopes and curvatures in this region have signs opposite to the case illustrated in Figure 14. Hence, the first bump has to be followed by a second one of smaller amplitude and opposite orientation. Continuation of this process generates the wavy deformation pattern, as found in numerical and analytical solution. For larger deformations the bending moments near the support are much stronger and the zone in which bending effects can be felt extends further into the shell.

It should be noted that the w term corresponds to the shell circumferential membrane stresses and that the w'''' term represents the axial bending moments. The interaction of these two quantities is a characteristic feature of the cylindrical shell geometry. A flat plate deforms smoothly near its clamped ends since (for small deformations) bending moments and midplane stresses are uncoupled. In this context it should be noted that a cylindrical shell whose radius tends to infinity does not approach the behaviour of a flat plate. The only important dimensionless geometrical parameter governing the behaviour of the shell is the radius-to-thickness ratio, R_0/h. Increasing the radius is therefore equivalent to reducing the shell thickness. In the limit, $R_0/h \to \infty$, the shell behaves like a membrane shell as the bending stiffness vanishes.